COMPUTATIONAL STUDY OF $LiMn_2O_4$ AS CATHODE MATERIAL IN Li-ION BATTERY

by

Kailin Fu

B.S. in Material Science & Engineering, South China University of Technology, 2012

Submitted to the Graduate Faculty of

Swanson School of Engineering in partial fulfillment

of the requirements for the degree of

Master of Science

University of Pittsburgh

2014

UNIVERSITY OF PITTSBURGH

SWANSON SCHOOL OF ENGINEERING

This thesis was presented

by

Kailin Fu

It was defended on

March 28th, 2014

and approved by

Guofeng Wang, PhD, Assistant Professor, Department of Mechanical Engineering and Material Science

Jung-Kun Lee, PhD, Associate Professor, Department of Mechanical Engineering and Material Science

Scott X. Mao, PhD, Professor, Department of Mechanical Engineering and Material Science

Thesis Advisor: Guofeng Wang, PhD, Assistant Professor, Department of Mechanical Engineering and Material Science

COMPUTATIONAL STUDY OF $LiMn_2O_4$ AS CATHODE MATERIAL IN Li-ION BATTERY

Kailin Fu, M.S.

University of Pittsburgh, 2014

Density functional theory (DFT) in spin polarized generalized gradient approximation with Hubbard U correction (GGA+U) was used to investigate the structural changes and voltages of $LiMn_2O_4$ cubic spinel during the electrochemical process in Li-ion battery. Jahn-Teller distortion and electrons transfer between Mn atoms and O atoms were observed by analysis the charge density. Effect of the reduction of Li content on distribution of Mn^{3+} and Mn^{4+} was also discussed. The low-index surface facets (100) and (111) extracted from the optimized bulk $LiMn_2O_4$ were calculated to study their structures and stability. Two possible terminations and some reconstructions of each surface were inspected. A specific reconstruction that would create a partial inverse spinel arrangement was applied on (111) surface and resulted in the most stable facet among the investigated facets. Furthermore, the negative charged vacancy formation energy indicated lithium extracted as a form of Li^+ ions, rendered the electron left in the bulk to drift through external circuit.

TABLE OF CONTENTS

LIST OF TABLES

LIST OF FIGURES

ACKNOWLEGMENT

I am very grateful to my advisor, Dr. Guofeng Wang. He provides the device and software license so that I can do this research. Moreover, I thank the members of his group, especially, Yingkai Lei, and Zhenyu Liu, for giving a lot of help in my thesis.

I express my gratitude to my thesis committee members, Dr. Jung-kun Lee, Dr. Scott X. Mao, for their attention and patience.

Finally, I have to express my extreme appreciation towards my parents for encouragement and support during my master study.

1.0 INTRODUCTION

Lithium-ion batteries have attracted lots of attentions, because of its various environmental usages from portable things, like mobile phones, iPads, laptops, and digital cameras, to electric vehicles. It has made our life more convenient and promoting the electronic industry. Moreover, the developments of smart phones and laptops request longer operating life in electronic devices with thinner and lighter Li-ion battery (LIB) of larger energy capacity and higher safety [1]. Though recent researches reported a rechargeable battery cell with over 30,000 cycles life at a relatively faster rate [2], increasement of the volumetric energy density is still a big challenge, and capacity fade is inevitable. The cycle life of the rechargeable battery is the

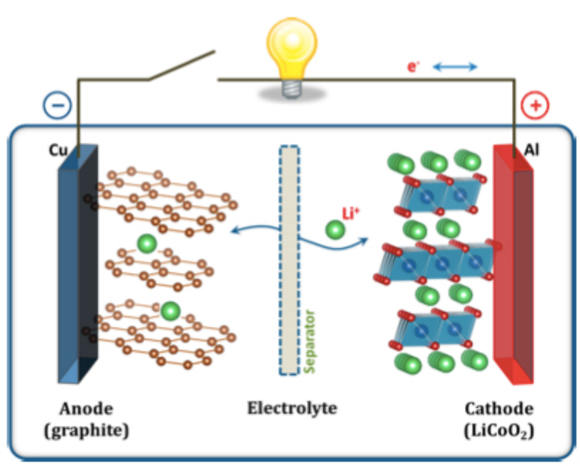

Figure 1 The first Li-ion battery [1].

number of cycles until the capacity fades to 80% of its premier value. Li-ion battery is made up of electrolyte and two electrodes, a reductant (anode) and an oxidant (cathode); the construction of the first LIB is shown in Figure 1. Commonly, lithium metal, graphite, silicon nanotubes, and alloys of Tin or lead, are used as anode materials, while, $LiCoO_2$, $LiNi_{1-x}Co_xO_2$, $LiMn_2O_4$, and $LiFePO_4$, are commonly used as cathode materials. During charge process, Li^+ will be extracted reversibly over a finite solid-solution range in cathode, drift through the separator in the electrolyte and be stored in the anode, vice versa in discharge process. For example, a LIB with graphite anode and $LiMn_2O_4$ cathode, the reactions during charging are:

$LiMn_2O_4 = xLi^+ + xe^- + Li_{1-x}Mn_2O_4$ in cathode

$xLi^+ + xe^- + C_6 = Li_xC_6$ in anode

Electrode-electrolyte chemical reactions would result in the irreversible formation of a passivated solid-electrolyte interphase (SEI) layer on an electrode during an initial charge of a cell fabricated in a discharged state.

The lithium manganese spinel $LiMn_2O_4$ is a kind of commercial cathode material for rechargeable LIB due to its performance, low cost and nontoxicity. There are commercial products in lithium manganese oxide system, such as $Li_xC/Li_{1-x}Mn_2O_4$ (3.5 V lithium-ion cells); $LiAl/Li_xMnO_2$ (2.6 V coin cells); $Li_{4+y}Ti_5O_{12}/Li_{1-y}MnO_2$ (1.5 V coin cells) [3]. The theoretical specific capacities of $LiCoO_2$, $LiMn_2O_4$ and $LiFePO_4$ are 273 mAh/g, 297 mAh/g and 170 mAh/g, respectively. Compared to $LiCoO_2$, $LiMn_2O_4$ is more thermal stable and safer. $LiMn_2O_4$ is a cubic spinel with space group symmetry $Fd\bar{3}m$. The lithium ions are positioned on the 8a tetrahedral sites of the structure, the manganese ions are located on the 16d octahedral sites, and the oxygen ions occupy the 32e positions. The lattice of $LiMn_2O_4$ is illustrated in Figure 2. The framework of this kind of stable spinel provided a stable host structure for the electrochemical insertion and extraction of lithium. The theoretical capacity of the $LiMn_2O_4$ is approximately 140 $mAhg^{--1}$ in the voltage range of 3.0-4.3 V. However, the stoichiometric $LiMn_2O_4$ is found to have lower capability. The lattice volume changes when charging. In this work, I have studied to use density functional theory (DFT) to investigate the structure changes and voltages of $LiMn_2O_4$ cubic spinel as a function of lithium content, and the electrons transfer in the bulk during charge process, and calculate the properties of the $LiMn_2O_4$ such as surface energies.

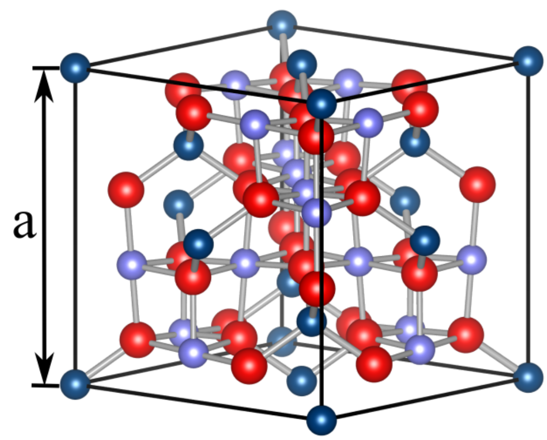

Figure 2 The bulk model of the $LiMn_2O_4$ structure illustrating the position of the Li (blue), the Mn (violet) and O (red) atomic species.

2.0 BACKGROUND

2. 1 LITHIUM ION BATTERY RESEARCHES

2.1.1 Experimental Researches

In order to improve the performance of cathode material in LIB, lots of experiments are carried out concerning the phase transformation, particle size, reaction between cathode and electrolyte, doping or coating to optimize structure, etc. $LiCoO_2$ is the first material used as cathode materials in LIB, whose theoretical capacity is about 274 mAh/g, but practically is found to be only 120-130 mAh/g in voltage range 2.7-4.2 V [4,5]. Shaju *et al*. [6] prepared the layered $Li(Ni_{1/3}Co_{1/3}Mn_{1/3})O_2$, by doping Ni and Mn into $LiCoO_2$ stucture, which gives an initial discharge capacity of 160 mAh/g in the range, 2.5-4.4 V at a specific current of 30 mA/g and a discharge capacity of 215mAh/g at lower current(10 mA/g) and in the voltage window 2.5-4.7 V. Zhang *et al*.[7] demonstrated the $LiMn_2O_4$ (LMO) is more thermostable than Li_xNiO_2 and Li_xCoO_2. Since LMO showed less energy and less sensitivity to changes in x, while reaction energy of Li_xNiO_2 and Li_xCoO_2 strongly depends on the change of x, thus the stoichiometry of these two materials required strictly control to achieve safety. Although LMO is cheap, environmentally friendly and has an acceptable high cycling capacity, capacity fading is the well-known significant problem. It is believed the reasons for capacity fade are surface chemistry of the electrode-electrolyte interface and the phase transformation during lithium extraction/insertion. The conventional wisdom being that Mn ions on the spinel surface dissolved into electrolyte following disproportion of Mn^{3+} through the Hunter reaction [8]:

$$2\ Mn_{solid}^{3+} \rightarrow Mn_{solid}^{4+} + Mn_{solution}^{2+}.$$

Mn^{2+} ions transfer through electrolyte and deposite both on and in the graphite anode. The Li content in the anode is depleted, hence the overall cell capacity faded. Moreover, Park *et al.* suggested that loss of the active material results in decreased effective transport properties in the cathode, and therefore lead to reduction in the electrochemical reaction rate and capacity [9]. Structural stability has been demonstrated to be an important factor for capacity fades. Huang *et al.* [10] introduced an nonstoichiometric spinel $Li_{1.03}Mn_2O_{4.04}$($Li_1[Mn_{1.98}Li_{0.02}]O_4$) contrast the stoichiometric spinel $LiMn_2O_4$ in structure change during cycling. The result shows that nonstoichiometric spinel remains single phase and capacity maintains good giving rise to high performance, stoichiometric spinel experiences structural degradation, involving accumulation of a second phase during cycling bringing large capacity losses. Cho and his co-worker [11] confirmed the capacity fading is related to the phase transition accompanying non-uniform strain during charge/discharge process. They successes to introduce a zero-strain cathode material, which is $LiCoO_2$ powder coated by a thin film of high fracture toughness metal oxides, like ZrO_2, to suppress the lattice constant changes during cycling. Besides, early studies proved the electrode of LIB is reactive in the presence of electrolyte at elevated temperature. MacNeil *et al.* [12] suggest that the $LiFePO_4$ is the safest material compared with a groups of 7 materials including $LiMn_2O_4$, LiNiO and $LiCoO_2$, and $LiMn_2O_4$ is the third safest following $LiFePO_4$ and $Li[Ni_{3/8}Co_{1/4}Mn_{3/8}]O_2$. Zaghib et al. [2] reported a novel LIB with a fast charge rate, long cycling life and safety is made up of nanoparticles of $LiFePO_4$ (LFP) covered with 2 wt.% carbon as cathode material and $Li_4Ti_5O_{12}$ (LTO) as a anode material. This battery is equipped in cars presented at the World Energy Council (Monteal, Sep. 2010), and it announced that charging time is just 5 minutes with three levels charger in parallel. Recent studies found the advanced electrode material for high power LIB, such as $LiFePO_4$ coated $LiMn_{1.5}Ni_{0.5}O_4$, which performs high energy density, due to the coating resists the inner particles reacting with electrolyte, and hence, prevents the formation of the passivated SEI layer and increase the safety of LIB [13]. However, Edström *et al*.[14] have proved that the surface film does not passivate the cathode surface, as in the case of anode, where the first-discharge SEI layer covered the entire electrode. Other researches found that reduction the size of the active particles of the electrodes to nanoscale could improve the power density, because the increased contact of surface with electrolyte. However, high energy density and high power density cannot achieved at the same time, thus it is suggested that in near future LIB will be confronted to the choice between them.

2.1.2 Computational Researches

Computational has a significant advantage that is scalability [15]. By solving the basic equations of quantum mechanics and statistical mechanics, computational method would determine the properties of the material and help to design and optimize materials. The most attractive concerns about LIB are voltage, capacity, cycle life, charge rate, safety and cost. For this paper just considers cathode material, the following properties would just analyze related to cathode. Computational study requires connection of macroscopic properties with microscopic behavior. The cathode materials with lower chemical potential for lithium, result in higher battery voltage. Capacity is related to the amount of Li ions reversibly inserting into and extracting from the cathode. Weight and volume density of lithium stored in cathode material ensure the cycle life required by applications. Provide that Li ions and electrons move fast in the cathode, the charge rate would be fast and higher power density responses out of the battery. Finally, safety is related to thermal stability and oxidation strength of the material [16], and cost of cathode material must less than $15-$20 per kg in order to meet automotive targets. Morgan et al. [17] calculate the activation barrier for Li motion in $LiFePO_4$ cathode is very small, indicating Li transfer very easy, thus predicting a extremely fast charging and discharging rate. The prediction was confirmed by experiments [18] latter, which reported a small battery with this material could be fully charge in 18 seconds. Ceder *et al*. present a method to calculate oxidation strength of $LiFePO_4$ and $LiMnPO_4$, by computed Li-Fe-O-P phase diagram and the reduction path of $FePO_4$ and $MnPO_4$. The results show the $LiFePO_4$ is rather safe, in the opposite, $LiMnPO_4$ is predicted not be safe as $LiFePO_4$, which is agree with the experimental measurements publish latter [19,20]. Let's take the following research as an example of using computational method to design a material. $Li(Ni_{0.5}Mn_{0.5})O_2$ is said to be a perfect cathode material in theory, but the charge rate is low and it loses much capacity at the charge/discharge rates. Ceder *et al*. assumed a structure with no nickel in the lithium layer, and the calculation results show this structure lower the activation barrier for Li motion, hence improve the rate. Fortunately, the hypothetical material was successfully synthesized [21]. Early researches use computational method to calculate the voltage and electron structure of the doped LMO [22,23], and to model the nanowire or nanorode structures [24,25] of the cathode material. Recently, researchers begin to study the Li migration path and surface properties. Ouyang et al. [26] found that LMO (100) surface coated with Al_2O_3 improves the performance of LMO cathode in LIB using DFT simulation. Karim *et al*. [27] drawed an equilibrium particle deduced from surface energies calculation, and the shape of the particle is total agree with experimental observation. Nakayama *et al*. [28] reported the Li migration path for LMO and the energy profile. They also confirmed that LMO with transition metal doping would improve the Li diffusivity. Furthermore, how the distribution and number of Mn^{3+} and Mn^{4+} ions affect the Li^+ ions diffusivity, was investigated by Meng *et al*. [29]. In future, computational method will continue aiding material design and will be accepted by more scholars.

2.2 DENSITY FUNCTIONAL THEORY

Density functional theory (DFT) is a first principle or ab initio method based on quantum mechanics. Nowadays, widely increasing uses of DFT method in chemistry, physics, material science, biochemistry and many branches of engineering, are due to its good accuracy and efficiency. For instance, DFT have been used to elucidate that defects promote reactivity for epoxidation of propylene in titanosilicalite (TS-1) catalysts [30], the role of vacancy and holes in the fracture of carbon nanotube [31], and properties of iron under the extreme pressures and temperatures as the Earth's interior [32]. Although DFT method is much better than the traditional multiparticle wave-function methods when applied to systems of many particles, computing time rises with the number of atoms [33]. Therefore, it is not suggested to use in a system with larger than 100 atoms in practice. A brief overview of the fundamentals of density functional theory is illustrated below.

2.2.1 Schrödinger's Equation

In quantum mechanics, we use Schrödinger equation instead of the equation of motion in classic mechanics to describe the change of quantum states with time. Since the mass of a proton or neutron in a nucleus is 1800 times greater than an electron, the nucleus can assume to be fixed, and just the electron moves. The respective mathematical problems can be solved separately by using Born-Oppenheimer approximation [34]. The time-independent Schrödinger equation then is simplified:

$$\hat{H}\Psi = E\Psi$$

where Ψ is the electronic wave function, and E is the ground-state energy. For a system with N electrons and k nuclei, where multiple electrons are interacting with multiple nuclei, the Hamiltonian, Ĥ, is defined as the following equation:

$$\hat{H} = -\frac{\hbar^2}{2m_e}\sum_{i=1}^{N} v_i^2 + \sum_{i=1}^{N}\sum_{j=1}^{k} V_j(r_i) + \frac{1}{2}\sum_{i=1}^{N}\sum_{j\neq i}^{N}\frac{e^2}{|r_i - r_j|}$$

The terms in the Hamiltonian are the kinetic energy of electrons, the interaction energy between each electron and all nuclei, and the interaction energy between electrons, respectively.

2.2.2 Exchange-Correlation Functional

Exchange-correlation functional, $E_{xc}[n(r)]$, accounts for the difference between the exact ground-state energy and the energy calculated in a Hartree approximation and the form of it is still unknown. Thus, effective approximations for $E_{xc}[n(r)]$ are required.

The local density approximation (LDA) is the simplest but remarkable useful approximation [33].

$$E_{ex}^{LDA} = \int e_{xc}[n(r)]n(r)dr$$

In the equation above, $e_{xc}[n(r)]$ is the exchange-correlation energy per particle of a homogeneous electron gas of density n. $e_{xc}[n(r)] = -\frac{3}{4}\left(\frac{3}{\pi}\right)^{\frac{1}{3}} n^{\frac{1}{3}}(r)$.

LDA is good for material with uniform electron gas system, and slow varying electron density, like metal. Practically, LDA overestimates energies, but it always agrees with geometric experimental data of molecules and solids.

The generalized gradient approximation (GGA) is not well defined as LDA, but it has a similar form as LDA. It takes into account the gradient of the density at the same coordinates.

$$e_{xc}(r) = e_{xc}[n(r), \nabla n(r)]$$

Here, $\nabla n(r)]$ is a gradient of the electron density, and it is good to represent surfaces where the electron density undergoes big difference. In theoretic, GGA is suitable for large density gradient system, like surface, an insulated molecular or atom. Experiences have shown that GGA is more accurate than LDA, but it often underestimates energies, and results in overestimate lattice parameters. There are two most common GGA functional, Perdew-Wang (PW91) functional [35] and the Perdew-Burke-Ernzerhof (PBE) [36] functional.

2.2.3 Pseudopotentials

Pseudopotential is used to replace the Coulomb potential of the nuclei and the effect of tightly bound core electrons by an effective potential acting on the valence electrons. The electron density of the core electron is replaced with a smoothed density that approach to the true core. Because the wave functions of all the electrons are very complicated, and the chemical behavior of the elements and material properties are mainly determined by the outermost valence electrons, in order to simplify the calculation, a frozen core approximation is applied. There are three kinds of pseudopotentials: norm-conserving pseudopotentials (NCPP), ultrasoft pseudopotentials (USPP), and projector augmented wave (PAW) pseudopotentials. NCPP is rarely used todays, and PAW are used most frequently. USPP would be used for speed up calculation, and for many system, it gives similar results as PAW gives. PAW is the most accurate in these three, and it gives reliable results in most systems including systems with strong magnetic moments or large difference in electronegativity.

2.2.4 GGA+U

Both LDA and GGA introduce a electron self-interaction energy error, in some case, this error would be cancelled between the different calculations that are combined into a property. However, in transition metal oxide, the electrons in d or f orbitals present a particularly large self-interaction energy, which cannot be cancelled. As a result, GGA+U method is used to correct the self-interaction error on transition metal oxides. GGA+U method would give correct magnetic ground states, electronic structure for systems and redox reaction energies in oxides [37]. The value of U can be obtained by fitting to experimental binary formation enthalpies [38], and can be calculated by ab initio self-consistent calculation wave functions of the given system [39].

3.0 VOLTAGE AND LATTICE PARAMETERS OF LMO

3.1 COMPUTATIONAL METHODS

A cubic spinel structure cell containing eight formula units of $LiMn_2O_4$ was used in this work. All calculations were performed using the spin polarized generalized gradient approximations (GGA+*U*) to the density functional theory (DFT). The projected augmented wave (PAW) method, as implemented in the Vienna *ab initio* simulation package (VASP), represented core electron states. I use a cutoff energy of 550 eV and an 8×8×8 Monkhorst-Pack scheme to sample the Brillouin zone. The calculation convergence criterion is 10^{-6}, and the atomic would be relaxing until the force acting on each atom was smaller than 0.01 eV/Å. Since Mn ions have *d* electrons, the Hubbard *U* correction is introduced to describe the effect of them. In spinel structure, the *U* value of Mn^{3+} ions and Mn^{4+} ions are 4.64 and 5.04, respectively. Because Mn^{3+} and Mn^{4+} ions coexist in $LiMn_2O_4$, an effective *U* value of 4.84 was suggested by Meng *et al*. [29] to apply in rotationally invariant GGA+*U* approach. The atomic positions were relaxed to obtain total energy and optimized cell structure. The equilibrium structures of $LiMn_2O_4$ were obtained from a series of calculation in different volume. To calculate the volume change in electrochemical process, a supercell with one vacancy ($Li_{0.875}Mn_2O_4$) and four vacancies ($Li_{0.5}Mn_2O_4$) out of eight Li sites were created. Moreover, the cubic spinel structure Mn_2O_4 was also optimized to get the equilibrium lattice parameters. To obtain the atomic charge density difference and electronic density of state (DOS), first step is a static self-consistent calculation; then run a non-self-consistent calculation; last but not least, operate non-self-consistent calculation keeping charge density constant during minimization.

3.2 RESULTS AND DISCUSSION

3.2.1 Bulk Structure and Charge Density

Since bulk $LiMn_2O_4$ has $Fd\bar{3}m$ group space, all 8a sites are equal, indicating that whichever Li ion extracted will not differ the energy of the equilibrium state of $Li_{0.875}Mn_2O_4$.In my study, I extract the one in [0.75 0.25 0.75] position. During delithiation the original symmetry would be destroyed, thus, Li ion extracted from different sites may contribute difference in total energy. In my study, I tried 4 possibilities, and I got the lowest equilibrium energy when lithium were extracted from two face-centered sites and two diamond sites [0.75 0.25 0.75] and [0.25 0.75 0.75]. Jahn-Teller distortion is observed in $Li_xMn_2O_4$ ($0<x\leq1$) due to GGA+U method distinguish Mn^{3+} and Mn^{4+}. This effect often occurs in octahedral complexes such as MnO octahedral in LMO spinel. One electron of the Mn^{3+} ions occupies e_g orbital, and in order to remove the degeneracy involved in e_g orbital, Mn-O bond will be elongated or contracted. While in Mn_2O_4, Mn ions only exist as Mn^{4+}, Jahn-Teller distortion does not display.

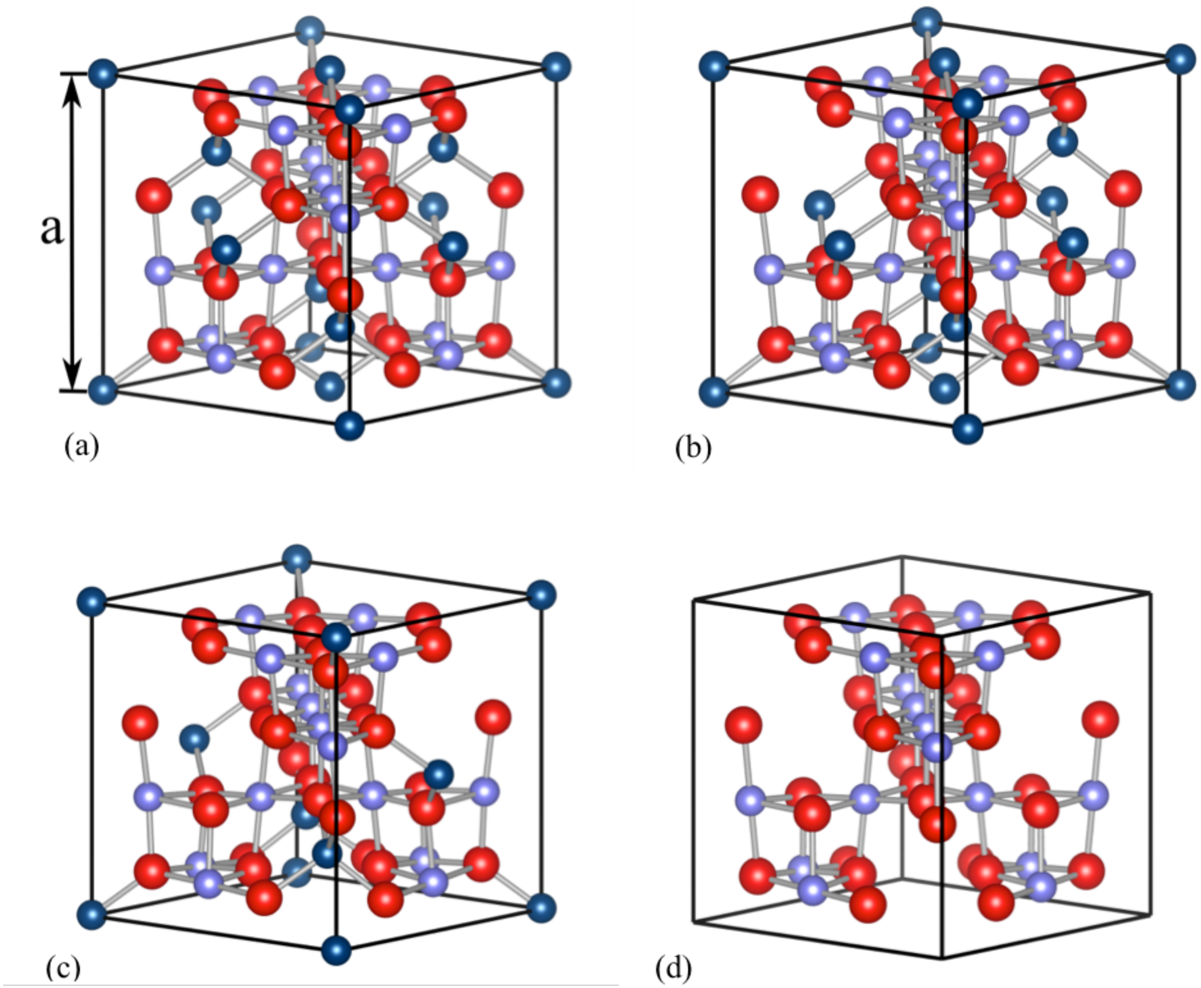

Figure 3 Equilibrium lattice structure of (a) $LiMn_2O_4$, (b) $Li_{0.875}Mn_2O_4$, (c) $Li_{0.5}Mn_2O_4$ and (d) Mn_2O_4, represented by Li (blue), Mn (violet) and O (red) atoms and bonds.

As to observe the electrons transference and distribution associated with Li ion extraction, use atomic charge density difference before and after interactions between atoms. Figure 4 intuitively represents the electrons distributions, where blue orbitals express who lose electrons and yellow orbitals indicate who gain electrons. Mainly, electrons transfer from Mn ions to O ions. However, it shows no electron gain or loss on Li atoms, which may be explained as no reactions between lithium and other two elements. Therefore, Mn-O is a structural frame for store Li atoms.

In $LiMn_2O_4$ lattice, the electrons are lost from two e_g orbitals ($d_{x^2-y^2}$ and d_{z^2}) of Mn, and gained in O orbitals. And all of the Mn ions look like the same, as well as O ions. While one Li atom remove, the charge density around the Li vacancy change. Electrons leave from just one e_g orbital of all Mn ions except four far from the vacancy. The orbitals of Mn ions nearest vacancy even rotated. Though it seems that the Mn ions near vacancy loss fewer electrons than the ones far from vacancy, actually, this figure just qualitatively draw the charge density change. In fact, the calculation results tell the Mn ions near vacancy loss more electrons than the ones further away. Provided that four Li ions extract, Electrons move from both e_g orbital of all Mn ions except four of them. Moreover, in Mn_2O_4 lattice, shapes of the charge density change of all the Mn ions and O ions looks like the same as in $LiMn_2O_4$ lattice, but a little bigger.

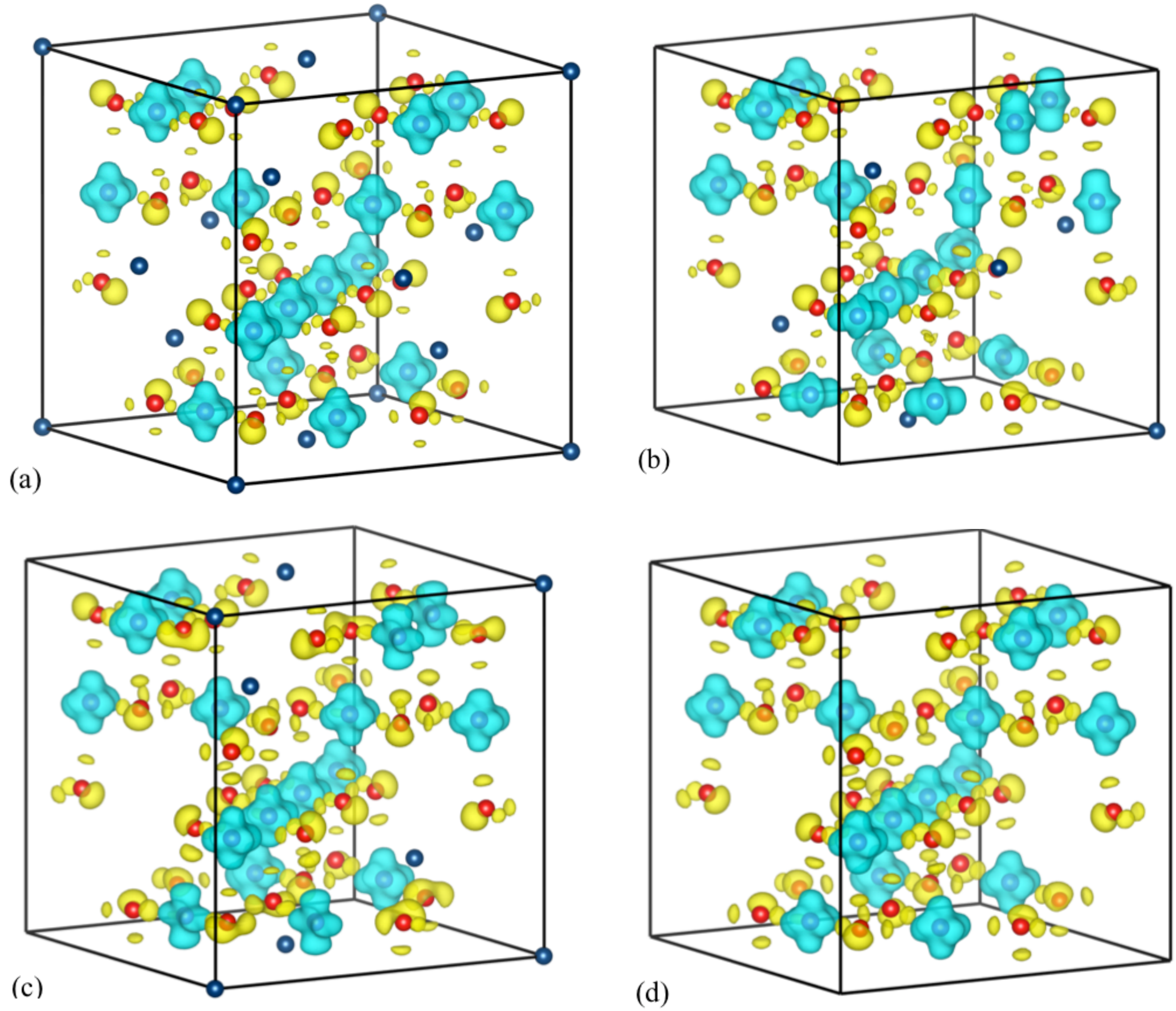

Figure 4 Charge density difference of (a) $LiMn_2O_4$, (b) $Li_{0.875}Mn_2O_4$, (c) $Li_{0.5}Mn_2O_4$ and (d) Mn_2O_4, where blue illustrate lose electrons and yellow indicate gain electrons. Isosurface is set to be 0.03.

3.2.2 Lattice Parameter and Voltage

Figure 5 shows the lattice constants of $Li_xMn_2O_4$ cubic cell as a function of Li concentration. At x=1, the result overestimates the lattice constant comparing to experimental observation by 3%, and comparing to other researchers who also use GGA+*U* method by less than 0.4%. The total volume change from $LiMn_2O_4$ to Mn_2O_4 is calculated as 5.4%, while experimental volume change is around 6-7%. It is a little underestimate the volume change. The smaller volume change during charge/discharge process, the better performance of cathode is.

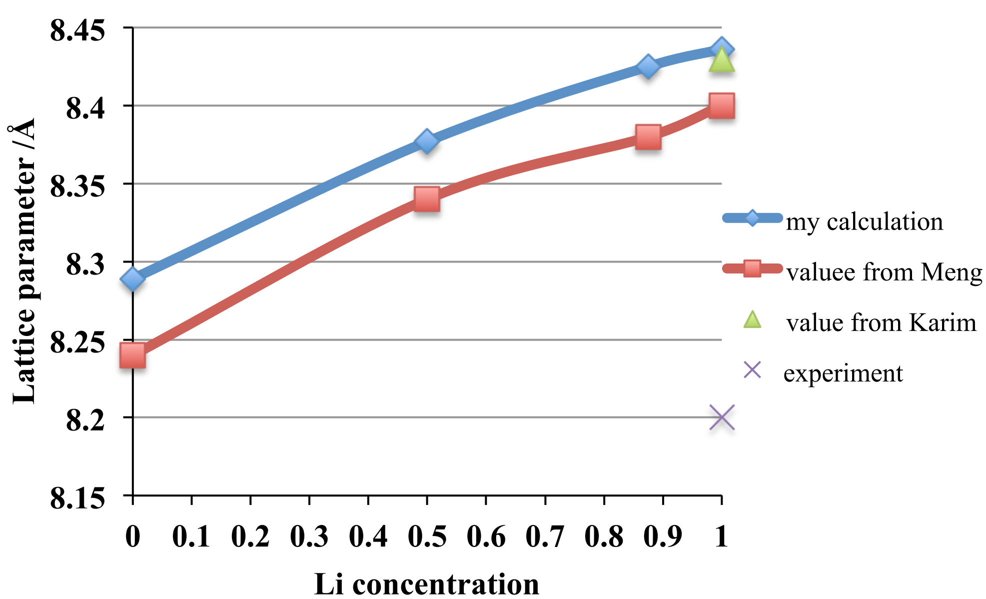

Figure 5 Calculated and experiment measured lattice parameters as a function of Li concentration.

In the charge and discharge process, the Li ions are extract from and insert into the cathode materials. The experimental studies have demonstrated that the lithium is extracted from the tetrahedral sites of the spinel structure at approximately 4 V in a two-stage process, separated by only 150 mV at a composition $Li_{0.5}Mn_2O_4$. The two-step process represented as voltage plateaus with a small voltage step is due to ordering of the lithium ions on one-half of the tetrahedral 8a sites. Voltage plateaus indicate two phases co-existent at certain Li concentration ranges. For any lithiation system, the total Gibbs free energy can be written as:

$$dG = -S\,dT + V\,dP + \sum_i \mu_i N_i$$

where S is entropy, T is temperature, V is volume, P is pressure, μ_i is chemical potential of element i and N_i is amount of element i. The chemical potential of the host elements (M) of the lithiation electrode materials do not change during the charge/discharge process. Thus the Gibbs free energy can be rewritten as:

$$dG = -S\,dT + V\,dP + \mu_{Li}\,dN_{Li} + \mu_M\,dN_M$$

If the system is isothermal and isobaric, the equation can be simplified to $dG = \mu_{Li}\,dN_{Li}$. Thus the chemical potential of Li ions can be calculated as $\mu_{Li} = dG/dN_{Li}$. From Nernst equation, the voltage of the cell can be expressed as

$$\text{Voltage} = -\frac{\mu_{Li}^{cathode} - \mu_{Li}^{anode}}{e}$$

where $\mu_{Li}^{cathode}$ is the chemical potential per atom of Li in the cathode, μ_{Li}^{anode} is the chemical potential per atom of Li in anode, and e is the absolute value of the electron charge, which is 1.602×10^{-19} C.

Because only one stable intermediate phase is found at x=0.5, indicating phase separations occur in two stages, $0\leq x\leq 0.5$ and $0.5\leq x\leq 1$. The chemical potentials of Li ions in both phase are equal in each stage, thus they can be approximated by:

$$\mu_{Li}^{LixMn2O4} = \frac{G_{Li0.5Mn2O4} - G_{Mn2O4}}{4}$$

and

$$\mu_{Li}^{LixMn2O4} = \frac{G_{LiMn2O4} - G_{Li0.5Mn2O4}}{4}$$

Li metal is used as the reference anode materials and the chemical potential in Li metal calculated at same conditions is μ_{Li}^{anode}= -1.9 eV. The voltage profiles is plotted in figure 6, compare with the results from Meng *et al.*. Two voltage plateaus were shown at 3.56 V and 3.95 V, which have 11% difference from the experimental value, 4.0 V and 4.15 V. The average voltage over all Li concentrations is 3.76 V. The absolute value of the voltage step is 390 mV, which is much larger than the 150 mV observed value.

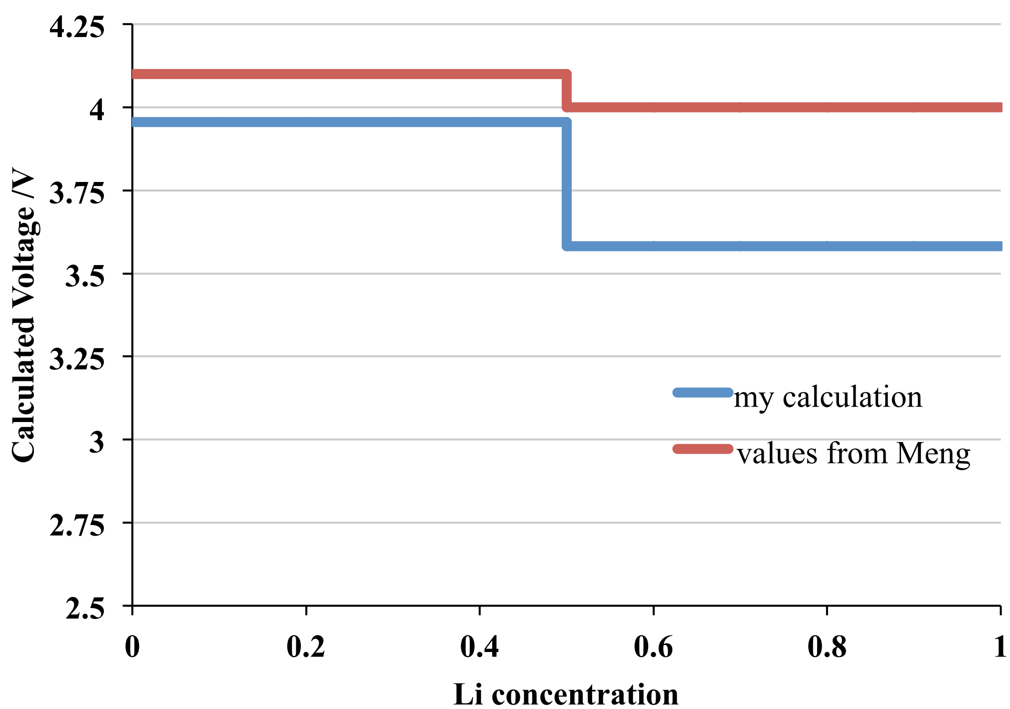

Figure 6 Voltage calculated by GGA+U method gain from my calculation and Meng et al.

3.2.3 Density of State (DOS)

Density of state (DOS) is used to analyze the electronic structure. Figure 7 shows the DOS of $LiMn_2O_4$, Li ions, Mn ions and O ions. The electronic states with energies no higher than Fermi energy are occupied, and the states higher than Fermi energy are empty. Since there are states with energies just little higher than Fermi energy, it exhibits as a conductor. However, it is actually a kind of semiconductor, the reason of this result needs further discussion. Mn and O ions contribute to the states less than Fermi energy, and it is indicated the bonds between Mn-O. Li ions contribute much in the empty states with much higher energies. In $LiMn_2O_4$, the average valence of Mn ions is +3.5. According to crystal field theory, Mn ions in the O octahedral leads to d orbitals splitting into two e_g orbitals with higher energy and three t_{2g}orbitals with lower energy. For Mn^{4+}, three valence electrons fill three t_{2g}orbitals, leaving e_g orbital empty, and there is a band gap between t_{2g} and e_g, thus Mn^{4+} ions operate as insulator or semiconductor. On the other hand, Mn^{3+} ion has four valence electrons occupy three t_{2g}orbitals and one e_g orbital. The band gap disappears, and it exhibits conductor properties. Thus in this material, only Mn^{3+} ions contribute to conduction, even though Mn^{3+} ions and Mn^{4+} ions coexist. The small peak near Fermi energy in Mn DOS is the e_g orbitals, and combined with the small peak near Fermi energy in O DOS makes the peak appear near Fermi energy in total DOS. Therefore, the Mn-O network makes a significant contribution to conductivity. Recalling the bulk charge density difference figure, in $Li_{0.5}Mn_2O_4$ lattice, there are four Mn ions different from the others. These four Mn ions are Mn^{3+} ions, and sequential extraction of Li ions would decrease the conductivity. In Mn_2O_4 lattice, there are only Mn^{4+} ions, thus Mn element cannot contribute to conductivity.

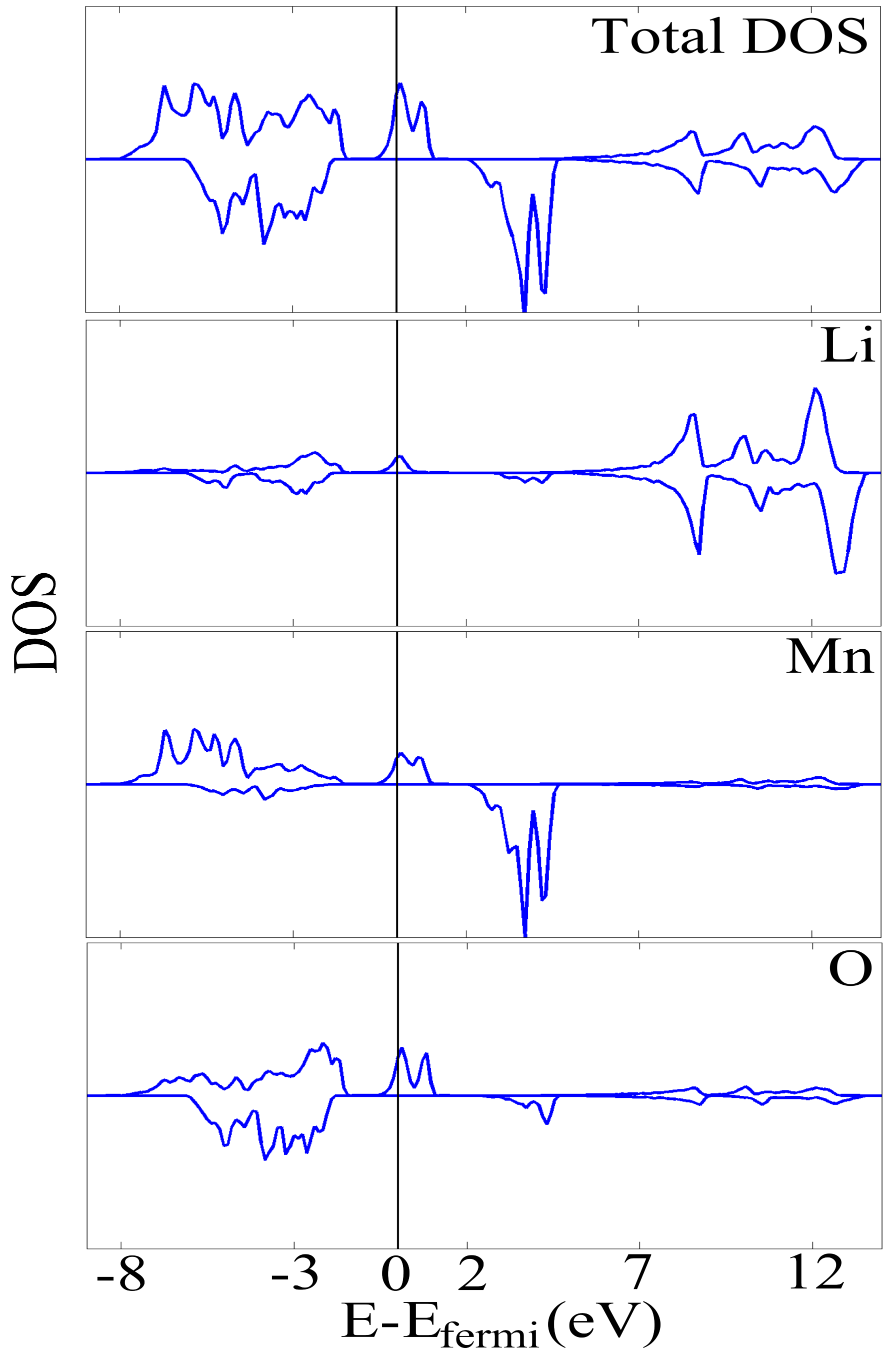

Figure 7 Density of state (DOS) of LMO and partial DOS of Li, Mn and O ions, with Fermi energy marked by a solid black line.

Furthermore, the charge density difference figure, Figure 4, shows no electrons gain or loss in Li atoms, which is total consistent with the result shown in DOS, Figure 7. From Figure 7, it is obvious that electrons in lithium make hardly contribution to the total valence band, and there are no bonds created between Li and O or between Li and Mn. There are two evidence demonstrate that lithium is reserved in Mn-O frame and has no chemical reactions with Mn and O.

3.3 CONCLUSION

During charge/discharge process, the extraction/insertion of the Li ions leads to volume changes of the LMO. The calculated voltages are little underestimated. Electrons distribution affected by Li vacancies could be illustrated by the charge density difference figure. Though, lithium is just stored in Mn-O frame, extraction of Li leads change in electrons distributions around the Li vacancies. DOS indicates the conductivity of LMO owing to the Mn-O octahedral network. When $x<0.5$, the conductivity of $Li_xMn_2O_4$ will reduce.

4.0 SURFACE PROPERTIES

4.1 COMPUTATIONAL METHODS

In this work, the same cubic spinel structure cell of $LiMn_2O_4$ was used. All calculations were performed using the spin polarized generalized gradient approximations (GGA+*U*) to the density functional theory (DFT). The projected augmented wave (PAW) method, as implemented in the Vienna *ab initio* simulation package (VASP), represented core electron states. A cutoff energy of 550 eV, and an effective *U* value of 4.84 were applied in rotationally invariant GGA+*U* approach. The lattice constant and the optimized structure obtained from the previous work were used to calculate the surface energies for the different surface facets of the $LiMn_2O_4$ spinel. The unrelaxed structures of (100) and (111) surfaces were extracted from the optimized bulk spinel structure. The surface energies of unrelaxed surface, γ, is computed as

$$\gamma = \frac{E_{slab} - NE_{bulk}}{2A}$$

where E_{slab} is the energy of the surface slab, E_{bulk} is the bulk energy per atom, *N* is the number of atoms in the surface slab, and *A* is the base area of the slab.

According to the Tasker criterion, both (100) and (111) surfaces have a net polar charge. Therefore, these surfaces require a redistribution or compensation of charges, such as additional Li ions, on reverse surfaces of the slab, which can be accompanied by a significant reconstruction of the surface atoms. When constructing the slab, a vacuum layers with a thickness about 8 Å was used along the surface normal, which sufficed to remove interaction between the slabs with 6 to 8 atomic layers. A calculation convergence criterion of 10^{-6} and the atomic force convergence criterion of 0.05 eV/Å were applied for the surface relaxations. Because of the complicated structure, several possible atomic terminations are possible, since the surface index does not specify where to cleave the surface. Thus this study investigated Li terminated (100), Mn/O terminated (100), Li/Mn/O terminated (111) and Li terminated (111) surfaces. Since (110) surface is well recognized as non-most-stable surface, and some calculation showed (100) surface to be the most stable facet, while some demonstrated (111) surface is the one. Therefore, I just discuss (100) and (111) surface, to study the reason for making such different results. For (100) surfaces studies, I used a slab of 8 atomic layers including 56 atoms, and the Brillouin zone was sampled by an 8×8×1 Monkhorst-Pack scheme. For (111) surfaces calculations, a slab of 6 atomic layers including 56 atoms was utilized, and an 8×4×1 Monkhorst-Pack scheme was applied in k-point sampling.

4.2 RESULTS AND DISCUSSION

4.2.1 Surface Configuration and Surface energy

Due to asymmetry charge on the two surface of a slab, for Li-terminated (100) surface, it needs to move one of the two surface Li ions from the top layer to the bottom one. Final structure is shown in Figure 8. From the top view, including two layers of Li atoms, it illustrates a very beautiful pattern. And it is obvious that it is the face-centered Li atom moved to the bottom.

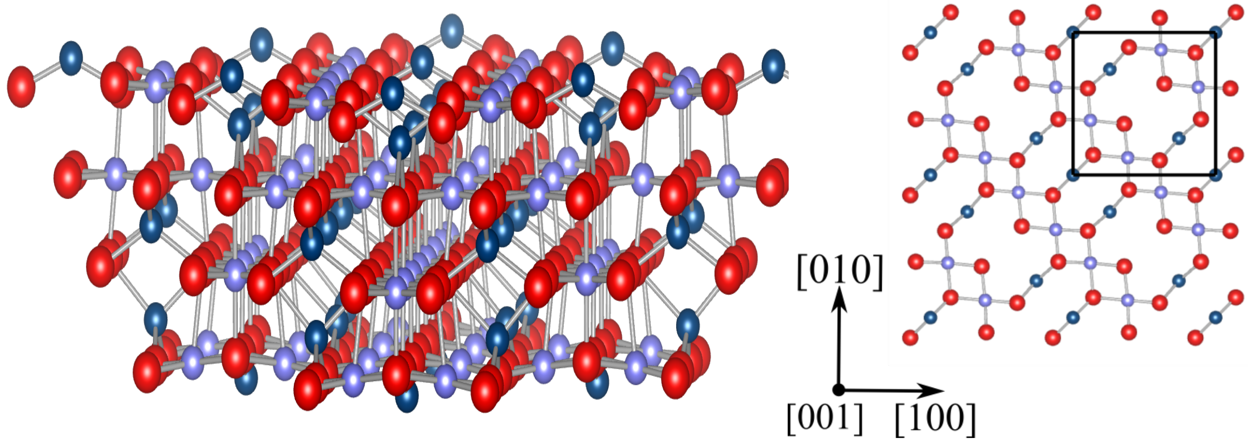

Figure 8 Li terminated (100) surface structure from some aspect (left), and the top layer of the surface (right) with directions and a unit cell framed in black line.

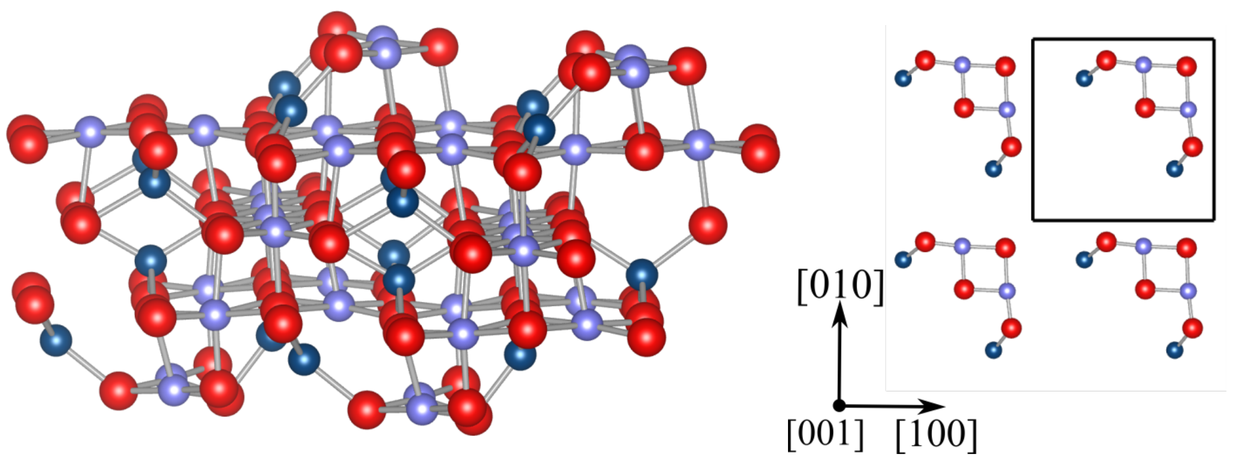

Figure 9 Mn/O terminated (100) surface from some aspect (left), and the top layer of the surface (right) with directions and a unit cell framed in black line.

For Mn/O terminated (100) surface, it need to move four O and two Mn from the top layers to the bottom, to eliminate the net charge. This configuration creates islands on the surface as shown in Figure 9. From the topside, only the atoms on the island are presented, and compared the unit cell with that in Figure 8, it is easily discovered which Mn and O atoms are moved. Another possible construction of the surface was calculated but has a higher energy than the one explained first. The calculated surface energies were found to be 0.40 J/m^2 and 0.90 J/m^2 for the Li and Mn/O terminations, respectively. Benedek et al. found that Li termination was the most stable surface, which suggesting it exhibits less broken bonds/area unit compared to the Mn/O termination [40].

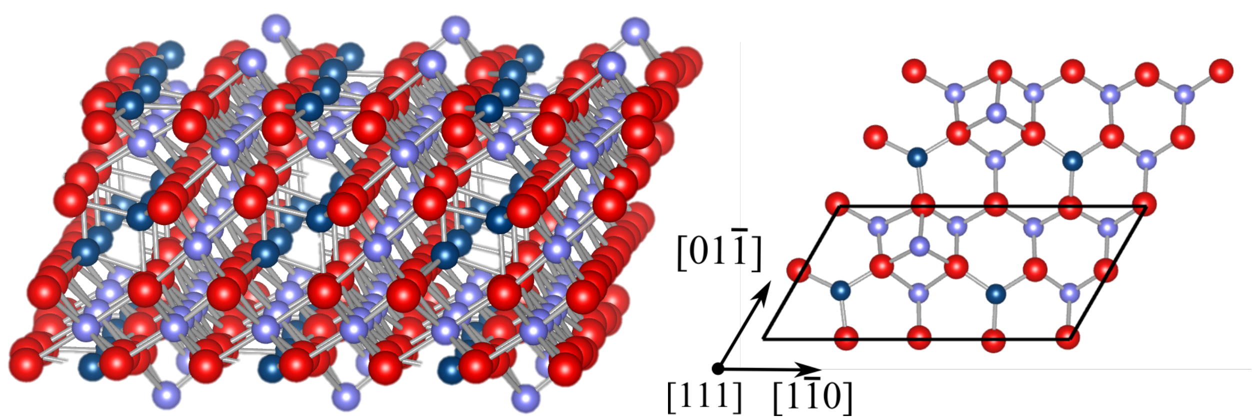

Figure 10 Li/Mn/O terminated (111) surface from some aspect (left), and the top layer of the surface (right) with directions and a unit cell framed in black line.

Li/Mn/O terminated (111) surface remains the original unreconstructed structure extracted from bulk relaxation, shown in Figure 10. It is apparently that (111) surfaces are much more density than (100) surfaces. The surface energy of Li/Mn/O terminated (111) surface is found to be 0.62 J/m^2, which is larger than Li terminated (100) surface. However, experimental work found the (111) facet is the predominant one in $LiMn_2O_4$ cubo-octahedral particles. Thus, it is believed that there should have a low-energy surface structure, which is reconstructed from the original one. According to Karim *et al*. [27], they exchange the undercoodinated surface Mn ions with Li from the next available layer, where Li occupy the octahedral site and Mn locates the tetrahedral sites. Figure 11 shows the reconstruction (111) surface and compared the view of the top layer with Figure 10 will find the exchanged Li atoms and Mn atoms. This reconstruction results in a local inverse spinel distribution at the surface. This kind of (111) surface reconstruction has been found to be stable for other spinel system like $MgAl_2O_4$ [41]. As a result, the surface energy of this reconstructed Li-terminated (111) surface is 0.33 J/m^2, which is the lowest surface energy. Thus it meets the agreement to the experiments, that (111) surface is the most stable facets in $LiMn_2O_4$.

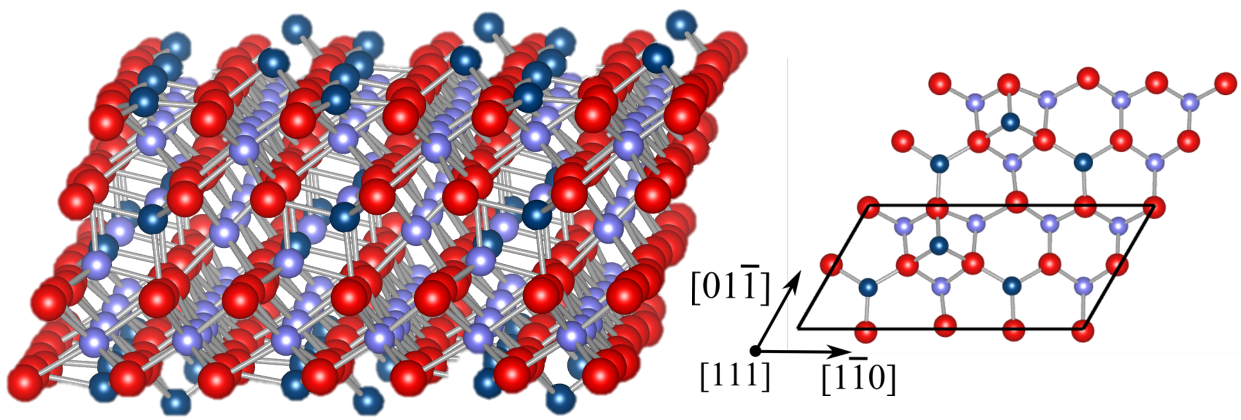

Figure 11 Li terminated (111) surface from some aspect (left), and the top layer of the surface (right) with directions and a unit cell framed in black line.

Surface energies of all the surfaces studied in this paper are list in Table 1, comparison with calculated values form other two papers. The surface energies vary obviously between studies (Benedek *et al*., and Karim *et al*.), may due to different structures and electronic/magnetic parameters like ferromagnetic or antiferromagnetic arrangement for Mn. However, the qualitative results that Li-terminated (100) surface is more stable than Mn/O terminated (100) surface, and that the reconstructed (111) surface is more stable than Li/Mn/O terminated (111) surface, are agree with all the studies.

Table 1 Calculated surface energies of (100) and (111) surface of LMO, with unit of (J/m^2).

	Surface energy	Karim *et al.*	Benedek *et al.*
Li terminated (100)	0.40	0.96	0.58
Mn/O terminated (100)	0.90	1.3	0.98
Li/Mn/O terminated (111)	0.62	1.23	1.29
Li terminated reconstructed (111)	0.33	0.67	0.85(Li/Mn terminated reconstructed)

4.2.2 Surface Charge Density

Study the charge density on the surface helps to understand the surface reaction. Figure 12 shows the Li terminated and Mn/O terminated (100) surfaces charge density difference, where blue orbitals express who lose electrons and yellow orbitals indicate who gain electrons. The shapes of orbitals, which lose or receive electrons, distinguish surface atoms and bulk atoms. Electrons only loss from $d_{x^2-y^2}$ orbitals of Mn, which is parallel to the surface, on both Li terminated and Mn/O terminated (100) surface, while electrons loss from $d_{x^2-y^2}$ and d_{z^2} orbitals of Mn atoms inside the bulk. As electrons move from Mn to O ions, the shape of O orbitals also changes a little bit. It seems that on the surface, O atoms obtain more electrons on the surface than inside the bulk, suggesting that Mn ions are willing to be higher valence on the surface.

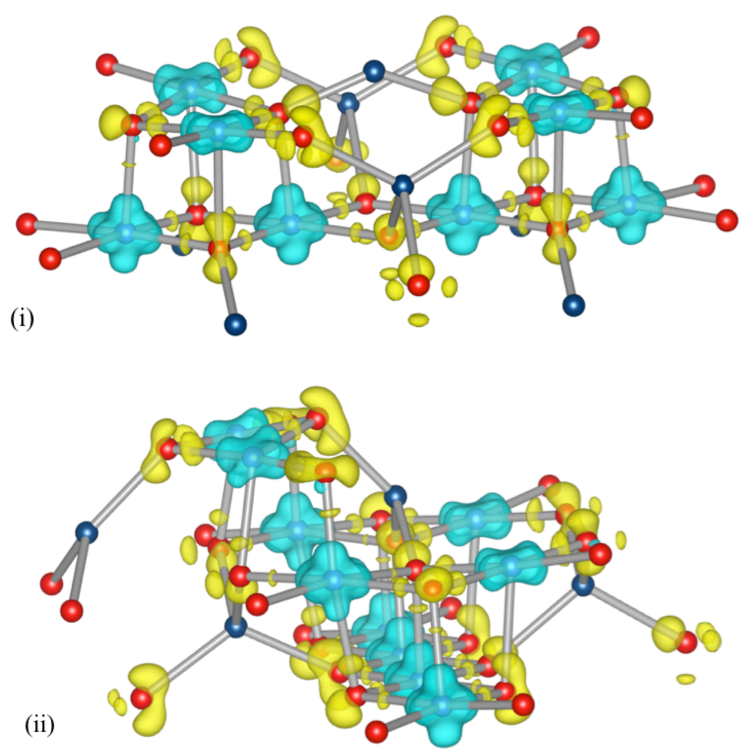

Figure 12 Charge density difference of (i) Li terminated and (ii) Mn/O terminated (100) surface, where blue represent lose electrons and yellow indicate gain electrons. Isosurface is set to be 0.03.

For (111) surface as shown in Figure 13, orbitals of two Mn ions near the surface layer are different from other Mn ions on the same layer. The two specific Mn ions locate at disparate positions in two kinds of (111) surface structures.

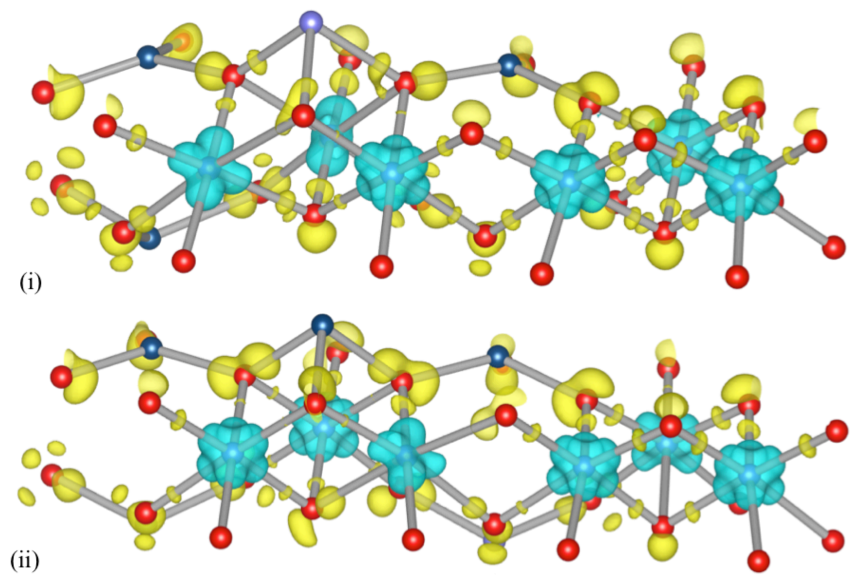

Figure 13 Charge density difference of (i) Li/Mn/O terminated and (ii) Li terminated reconstructed (111) surface, where blue represent lose electrons and yellow indicate gain electrons. Isosurface is set to be 0.03.

4.3 CONCLUSION

The significantly difference of the absolute energies from my calculation to Karim *et al.* and Benedek *et al.*, due to the difference in structure and the electronic/magnetic parameters. In my work I used the structure Karim *et al.* suggested, but employed a ferromagnetic arrangement for Mn ions like Benedek *et al*. did, while Katim *et al*. applied an antiferromagnetic arrangement. Though the quantities do not agree to each other, the qualitative analysis is reliable. In DFT study, a precise structure is the most significant element to achieve credible results.

5.0 CHARGED VACANCY

5.1 COMPUTATIONAL METHODS

Charged vacancy can be easily achieve by added an electron to the total net electrons in a bulk with a vacancy. Then run a calculation using the same method as previous bulk LMO with a Li vacancy calculation. To obtain the charge density, self-consistent calculation is operated following by a non-self-consistent calculation with and without keeping the charge density constant during minimization.

5.2 RESULTS AND DISCUSSION

All of my LMO bulk calculations are assumed that extraction of Li ions leaves neutral vacancy. However, charged vacancy commonly exist in compound, and vacancy with or without charged is determined by the form of the leaving atom. In fact, vacancy with a negative charge is created by Li^+ leave, and vacancy with no charge is made by Li atom extract. To investigate the influence of addition charge in vacancy, vacancy formation energy is introduced.

Vacancy formation energy:

$$\Delta E_f = E^q - E^{perf} + \mu_{Li} + q\mu_e$$

where E^q and E^{perf} are the energy of the simulation cell with and without vacancy with charge state q; μ_{Li} is the chemical potential of Li; μ_e is the chemical potential of electron. In this study, q=-1 for charge vacancy and q=0 for neutral vacancy; μ_{Li} is approximated to the cohesive energy of metal Li, and since LMO is a kind of conductor, μ_e can be defined as Fermi energy.

As a result, the neutral vacancy formation energy is 2.891 eV, while the charged vacancy formation energy is 2.874 eV, which is smaller than the neutral one. Charged vacancy formation energy smaller than neutral vacancy formation energy indicated that charged vacancy is formed easier than neutral vacancy, thus lithium is more willing to be extracted as a Li^+ ions, rather than Li atom. But my result gives a very little difference in these two formation energies, which is not so convincible. Charge density difference of $Li_{0.875}Mn_2O_4$ with charged vacancy is also taken into account; nevertheless, the figure looks like the same as the one with neutral vacancy.

5.3 CONCLUSION

It is suggested that lithium is extracted as Li^+ ions, and the electrons left form free electrons going through the external circuit. Provided that electrons are added in bulk calculation, the results especially the voltage would more close to the experimental values. Although addition charge seems to be a good correction in calculation, no evident shows where and how the charge distributes. Whereas, calculations of Li atom and Li ion diffusion, are needed to improve reliability of my prediction.

BIBLIOGRAPHY

[1] John B. Goodenough and Kyu-Sung Park. The Li-ion rechargeable battery: a perspective. J. Am. Chem. Soc., 2013 135 (4): 1167-1176

[2] K. Zaghib, M. Dontigny, A. Guerfi, P. Charest, I. Rodrigues, A. Mauger, C. M. Julien. Safe and fast-charging Li-ion battery with long shelf life for power applications. J. Power Sources 2011, 196(8): 3949-3954.

[3] Micheal M. Thackeray. Manganese oxides for lithium batteries. Prog. Solid St. Chem. 1997 25(1): 1-71

[4] J. Fan, P.S. Fedkiw. Electrochemical impedance spectra of full cells: Relation to capacity and capacity-rate of rechargeable Li cells using $LiCoO_2$, $LiMn_2O_4$, and $LiNiO_2$ cathodes. J. Power Sources, 1998, 72 (2): 165-173

[5] A. Manthiram, J. Kim. Low temperature synthesis of insertion oxides for lithium batteries. Chemistiy of Matertials, 1998, 10 (10): 2895-2909

[6] K.M. Shaju, G.V. Subba Rao, B.V.R. Chowdari, Performance of layered $Li(Ni_{1/3}Co_{1/3}Mn_{1/3})O_2$ as cathode for Li-ion batteries. Electrochimica Acta. 2002, 48(2): 145-151

[7] Z. Zhang, D. Fouchard, J.R. Rea. Differential scanning calorimetry material studies: implications for the safety of lithium-ion cells. J. Power Sources, 1998, 70(1): 16-20

[8] James C. Hunter. Preparation of a new crystal form of manganese dioxide: λ-MnO_2. J. Solid State Chem., 1981, 39 (2): 142-147

[9] J. Park, J. H. Seo, G. Plett, W. Lu, A. M. Sastry. Numerical simulation of the effect of the dissolution of LiMn2O4 particles on Li-ion battery performance. Electrochemical and Solid-State Letters, 2011, 14(2): A14-A18

[10] H. Huang, C. A. Vincent, P. G. Bruce. Correlating capacity loss of stoichiometric and nonstoichiometric lithium manganese oxide spinel electrodes with their structural integrity. J. Electrochem. Soc.,1999, 146(10): 3649-3654

[11] J. Cho, Y.J. Kim, T.J. Kim, and B. Park. Zero-strain intercalation cathode for rechargeable Li-Ion cell. Angewandte Chemie, 2001, 113(18): 3471-3473

[12] D.D. MacNeil, Z. Lu, Z. Chen, J.R. Dahn, A comparison of the electrode/electrolyte reaction at elevated temperatures for various Li-ion battery cathodes. J. Power Sources 2002, 108(1): 8-14

[13] K. Zaghib, A. Mauger, H. Groult, J. B. Goodenough, C. M. Julien. Advanced electrodes for high power Li-ion batteries. Materials, 2013, 6(3): 1028-1049

[14] K. Edström, T. Gustafsson, J.O. Thomas. The cathode–electrolyte interface in the Li-ion battery. Electrochimica Acta, 2004, 50(2): 397-403.

[15] Gerbrand Ceder, Opportunities and challenges for first-principles materials design and applications to Li battery materials. MRS Bulletin, 2010, 35(9): 693-701

[16] L. Wang, T. Maxisch, G. Ceder. A First-Principles Approach to Studying the Thermal Stability of Oxide Cathode Materials. Chem. Mater. 2007, 19(3): 543-552

[17] D. Morgan, A. Van der Ven, G. Ceder. Li Conductivity in Li_xMPO_4 (M = Mn, Fe, Co, Ni) Olivine Materials. Electrochem. Solid-State Lett., 2004 7(2): A30-A32

[18] B. Kang, G. Ceder, Battery materials for ultrafast charging and discharging. Nature 2009, 458(7235): 190-193

[19] S.W. Kim, J. Kim, H. Gwon, K. Kang. Phase Stability Study of $Li_{1-x}MnPO_4$ ($0 \leqslant x \leqslant 1$) Cathode for Li Rechargeable Battery. J. Electrochem. Soc., 2009, 156(8): A635-A638

[20] G. Chen, T.J. Richardson. Thermal instability of Olivine-type $LiMnPO_4$ cathodes. J. Power Sources, 2010, 195(4): 1221-1224

[21] K. Kang, Y.S. Meng, J. Breger, C.P. Grey, G. Ceder. Electrodes with high power and high capacity for rechargeable lithium batteries. Science, 2006, 311(5763): 977-980

[22] S. Shi, D. Wang, S. Meng, L. Chen, X. Huang. First-principles studies of cation-doped spinel $LiMn_2O_4$ for lithium ion batteries. Physical Review B, 2003, 67(11): 115130

[23] R. Benedek, C.S. Johnson, M.M. Thackeray. First-principles calculations for Co-doped $LiMn_{1.5}Ni_{0.5}O_4$ and $LiMn_2O_4$ battery electrodes. Electrochemical and solid-state letters, 2006, 9(6): A289-A291

[24] F. Cheng, H. Wang, Z. Zhu, Y. Wang, T. Zhang, Z. Tao, J. Chen. Porous $LiMn_2O_4$ nanorods with durable high-rate capability for rechargeable Li-ion batteries. Energy & Environmental Science, 2011, 4(9): 3668-3675

[25] E. Hosono, T. Kudo, I. Honma, H. Matsuda, H. Zhou. Synthesis of Single Crystalline Spinel $LiMn_2O_4$ Nanowires for a Lithium Ion Battery with High Power Density. Nano letters, 2009, 9(3): 1045-1051

[26] C. Y. Ouyang, X. M. Zeng, Ž. Šljivancanin, A. Baldereschi. Oxidation states of Mn atoms at clean and Al2O3-covered LiMn2O4 (001) surfaces. J. Phys. Chem. C, 2010, 114(10): 4756-4759

[27] Altaf Karim, Sonia Fosse, and Kristin A. Persson. Surface structure and equilibrium particle shape of the $LiMn_2O_4$ spinel from first-principles calculations. Phys. Rev. B, 2013, 87 (7): 075322

[28]M. Nakayama, M. Kaneko, M. Wakihara. First-principles study of lithium ion migration in lithium transition metal oxides with spinel structure. Phys. Chem. Chem. Phys., 2012, 14(40): 13963-13970

[29]Bo Xu, Shirley Meng, Factors affecting Li mobility in spinel $LiMn_2O_4$ -A first-principles study by GGA and GGA+U methods. J. Power Sources, 2010, 195(15): 4971-4976

[30] D.H. Wells, W.N. Delgass, K .T.Thomson. Evidence of defect-promoted reactivity for epoxidation of propylene in titanosilicate (TS-1) catalysts: a DFT study. Journal of the American Chemical Society, 2004, 126(9): 2956-2962

[31] S.L.Mielke, D. Troya, S. Zhang, J.L. Li, S. Xiao, R. Car, R.S. Ruoff, G.C.Schatz, T. Belytschko. The role of vacancy defects and holes in the fracture of carbon nanotubes. Chemical Physics Letters, 2004, 390(4): 413-420

[32] L. Vočadlo, J. Brodholt, D. Alfè, G.D.Price. The structure of iron under the conditions of the Earth's inner core. Geophysical research letters, 1999, 26(9): 1231-1234

[33] W. Kohn. Nobel lecture: electronic structure of matter-wave functions and density functionals. Reviews of Modern Physice, 1999, 71(5): 1253-1266

[34] D.S. Sholl and J.A. Steckel. Density Functional Theory: A Practical Introduction. John Wiley and Sons, Hoboken, New Jersey, 2009

[35] J.P. Perdew and Y. Wang. Accurate and simple analytic representation of the electron-gas correlation energy. Physical Review B, 1992, 45(23): 13244

[36] J.P. Perdew, K. Burke, M. Ernzerhof. Generalized gradient approximation made simple. Phys. Rev. Lett., 1996, 77(18): 3865-3868

[37] A. Jain, G. Hautier, S.P. Ong, C.J. Moore, C.C. Fischer, K.A. Persson, G.Ceder. Formation enthalpies by mixing GGA and GGA+ U calculations. Physical Review B, 2011, 84(4): 045115

[38] L. Wang, T. Maxisch, and G. Ceder. Oxidation energies of transition metal oxides within the GGA+ U framework. Phys. Rev. B, 2006, 73(19): 195107

[39] A. N. Andriotis, R.M. Sheetz, M. Menon. LSDA+U method: A calculation of the U values at the Hartree-Fock level of approximation. Phys. Rev. B, 2010, 81(24): 245103

[40] R. Benedek and M.M. Thackeray. Simulation of the surface structure of lithium manganese oxide spinel. Physical Review B, 2011, 83(19): 195439

[41] S.C. Parker, P.M. Oliver, N.H. De Leeuw, J.O. Titiloye, and G.W. Watson. Atomistic simulation of mineral surfaces: Studies of surface stability and growth. Phase Transitions, 1997, 61(1-4): 83-107.